Comput. Methods Appl. Mech. Engrg. 273 (2014) 1–18

Contents lists available at ScienceDirect

Comput. Methods Appl. Mech. Engrg.

journal homepage: www.elsevier.com/locate/cma

Large deflection geometrically nonlinear analysis of carbon nanotube-reinforced functionally graded cylindrical panels

L.W. Zhang [a], Z.X. Lei [b,c], K.M. Liew [b,d,*], J.L. Yu [c]

[a] College of Information Technology, Shanghai Ocean University, Shanghai 201306, PR China
[b] Department of Civil and Architectural Engineering, City University of Hong Kong, Kowloon, Hong Kong Special Administrative Region
[c] CAS Key Laboratory of Mechanical Behavior and Design of Materials, University of Science and Technology of China, Hefei 230000, PR China
[d] City University of Hong Kong Shenzhen Research Institute Building, Shenzhen Hi-Tech Industrial Park, Nanshan District, Shenzhen, PR China

ARTICLE INFO

Article history:
Received 30 September 2013
Received in revised form 15 January 2014
Accepted 23 January 2014
Available online 5 February 2014

Keywords:
Nonlinear deflection
Carbon nanotube
Functionally graded cylindrical panel
kp-Ritz method

ABSTRACT

A large deflection geometrically nonlinear behavior of carbon nanotube-reinforced functionally graded (CNTR-FG) cylindrical panels under uniform point transverse mechanical loading is studied. The analysis is carried out using the kp-Ritz method with kernel particle function is employed to construct the shape functions for the two-dimensional displacement approximations. Based on the first-order shear deformation shell theory, nonlinear governing equations are developed with geometric nonlinearity taking the form of von Kármán strains. It is assumed that carbon nanotubes are uniaxially aligned in the axial direction and are functionally graded in thickness direction of the cylindrical panels. The effective material properties of resulting CNTR-FG panels are estimated by employing an equivalent continuum model based on the Eshelby–Mori–Tanaka approach. A stabilized conforming nodal integration scheme is employed to evaluate the system bending stiffness and the membrane as well as shear terms are calculated by the direct nodal integration method to eliminate shear locking, for a very thin cylindrical panel. Several numerical example problems are examined to reveal the influences of volume fraction of carbon nanotubes, span angle, edge-to-radius ratio and thickness on nonlinear responses of the CNTR-FG panels. Moreover, effects of different boundary conditions and distribution type of carbon nanotubes are also investigated.

© 2014 Elsevier B.V. All rights reserved.

1. Introduction

Carbon nanotube reinforced composite materials have received wide attention from researchers since carbon nanotubes (CNTs) have become potential constituents of reinforcements because they have been demonstrated to have high strength and stiffness with high aspect ratio and low density. Applications of carbon nanotube reinforced composite materials may expand in areas such as reinforcing composites, electronic devices and many others. Therefore, theoretical and numerical analyzes play an important role in capturing and understanding the fine mechanical properties of these carbon nanotube reinforced composite materials.

* Corresponding author at: Department of Civil and Architectural Engineering, City University of Hong Kong, Kowloon, Hong Kong Special Administrative Region. Tel.: +852 34426581.
E-mail address: kmliew@cityu.edu.hk (K.M. Liew).

http://dx.doi.org/10.1016/j.cma.2014.01.024
0045-7825/© 2014 Elsevier B.V. All rights reserved.

Earlier investigations about carbon nanotube reinforced composite materials were mainly focused on their material properties and constitutive modeling. Since the performance of a composite material system is highly dependent on the interfacial characteristics of the reinforcement and the matrix material, Liao and Li [1] reported a study on interfacial characteristics of a carbon nanotube reinforced polystyrene composite system through molecular mechanics simulations and elasticity calculations. They found that interfacial shear stress of the CNT-polystyrene system is about 160 MPa, significantly higher than most carbon fiber reinforced polymer composite systems. Wong et al. [2] examined the mechanical properties of CNT/polystyrene and CNT/ epoxy thin film. The results showed that these polymers adhered well to CNT at the nanometer scale and CNT-polymer interfacial shear stress (at 0 K) is about 138 and 186 MPa for CNT/epoxy and CNT/polystyrene, respectively. With 1 wt% nanotubes addition dispersed homogeneously throughout polystyrene matrices, tensile tests on composite films revealed 36–42% increase in elastic modulus and 25% increase in breaking stress, implying significant load transfer across the nanotube-matrix interface [3]. Odegard et al. [4] proposed that the nanotube, the local polymer near the nanotube, and the nanotube/polymer interface can be modeled as an effective continuum fiber by using an equivalent-continuum modeling method at small length scales. By using a multiscale approach, Gao and Li [5] developed a shear-lag model for carbon nanotube-reinforced polymer composites. With nanotube modeled at the atomistic scale and matrix deformation analyzed by the continuum finite element method, Li and Chou [6] reported a multiscale modeling of the compressive behavior of carbon nanotube/polymer composites. Seidel and Lagoudas [7] modeled the effective elastic properties of carbon nanotube reinforced composites by using a composite cylinders micromechanics technique conjunction with the Mori–Tanaka and self-consistent techniques.

Although the above investigations are quite useful for understanding of constitutive and material properties of carbon nanotube reinforced composite materials, the ultimate purpose of the development of this advanced class of materials is usage in actual structural applications. Since carbon nanotube reinforced composites may be incorporated in the form of beam, plate or shell as structural components, there is a need to observe the global response of carbon nanotube reinforced beam, plate or shell. Wuite and Adali [8] presented a multiscale analysis of deflection and stress behavior of nanocomposite reinforced beams by using micromechanics relations to determine the elastic constants in terms of nanotube volume fraction. With effective material properties estimated by rule of mixture model, Yas and Samadi [9] carried out free vibration and buckling analyses of nanocomposite Timoshenko beams reinforced by single-walled carbon nanotubes resting on an elastic foundation. Rafiee et al. [10] studied large amplitude free vibration of functionally graded carbon nanotube reinforced composite beams with surface-bonded piezoelectric layers subjected to a temperature change and an applied voltage. For carbon nanotube reinforced plate, Zhu et al. [11] carried out static and dynamic analyses of functionally graded carbon nanotube reinforced composite plates using the finite element method. Formica et al. [12] studied vibration behaviors of CNTRC plates employing an equivalent continuum model, in accordance with the Eshelby–Mori–Tanaka approach. By using the mesh-free kp-Ritz, Lei et al. [13–17] reported some typical mechanical analysis of functionally graded carbon nanotube reinforced composite plates and panels. With nanocomposite plates reinforced by single-walled carbon nanotubes resting on an elastic foundation, a large amplitude vibration analysis in thermal environments is presented [18]. By employing an equivalent continuum model based on the Eshelby–Mori–Tanaka approach, Aragh et al. [19] studied natural frequency characteristics of a continuously graded CNT-reinforced cylindrical panel. Shen and Xiang [20] investigated the large amplitude vibration behavior of nanocomposite cylindrical shells in thermal environments. Shen [21] presented thermal buckling and postbuckling analysis of nanocomposite cylindrical shells reinforced by single-walled carbon nanotubes subjected to a uniform temperature rise. Some further investigations about postbuckling analysis of nanocomposite cylindrical shells subjected to axial compression and lateral pressure were performed by Shen [22,23].

In this paper, a first attempt to study large deflection geometrically nonlinear behavior of carbon nanotube-reinforced functionally graded (CNTR-FG) cylindrical panels is carried out using the mesh-free kp-Ritz method based on a modified version of Sander's nonlinear shell theory to derive the discretized governing equations. With CNTs assumed uniaxially aligned in axial direction and functionally graded in thickness direction of the panels, the effective material properties of CNTR-FG cylindrical panels are estimated through a micromechanical model based on the Eshelby–Mori–Tanaka approach. To improve computational efficiency and eliminate shear and membrane locking, a stabilized conforming nodal integration scheme is employed to evaluate the system bending stiffness and the membrane; shear terms are calculated by the direct nodal integration method. A combination of the arc-length iterative algorithm and the modified Newton–Raphson method is adopted to solve the nonlinear system equations to track the full load–displacement path. Several computational simulation examples are presented to figure out the effects of volume fraction of CNTs, edge-to-radius ratio, span angle, thickness, boundary conditions and distribution types of CNTs on nonlinear responses of the CNTR-FG panels.

2. Carbon nanotube reinforced composite panels

A CNTR-FG cylindrical panel having the length L, radius R, span angle θ_0 and thickness h is shown in Fig. 1. A coordinate system (x, θ, z) is established on the middle surface of the panel. The panels are made of a mixture of single-walled carbon nanotubes (SWCNTs) and the matrix in which the CNTs are assumed to be uniaxially aligned in axial direction and functionally graded in thickness direction of the cylindrical panels (Fig. 2). According to distributions of CNTs in the thickness direction of cylindrical panels, CNT volume fractions $V_{CNT}(z)$ are in accordance with the law:

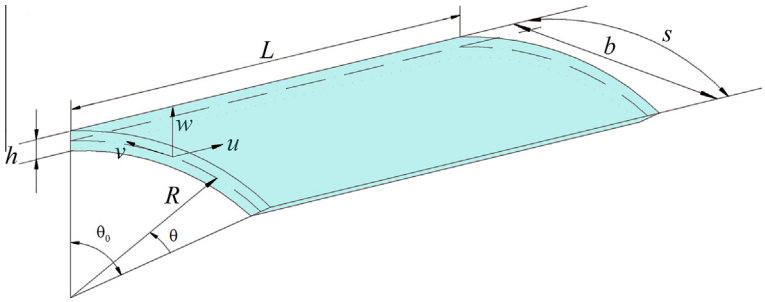

Fig. 1. Geometry properties of CNTR-FG cylindrical panel.

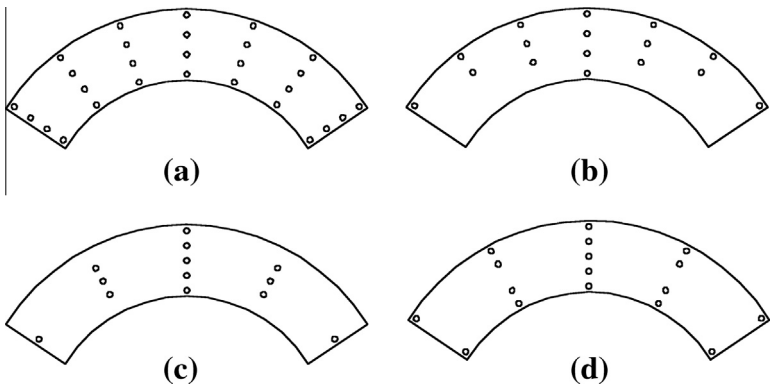

Fig. 2. Distribution types of CNTs of CNTR-FG cylindrical panels. (a) UD panel; (b) FG-V panel; (c) FG-O panel; (d) FG-X panel.

$$V_{CNT}(z) = \begin{cases} V^*_{CNT} & (\text{UD}) \\ \left(1+\frac{2z}{h}\right)V^*_{CNT} & (\text{FG-V}) \\ 2\left(1-\frac{2|z|}{h}\right)V^*_{CNT} & (\text{FG-O}) \\ 2\left(\frac{2|z|}{h}\right)V^*_{CNT} & (\text{FG-X}) \end{cases}, \tag{1}$$

where

$$V^*_{CNT} = \frac{w_{CNT}}{w_{CNT} + (\rho^{CNT}/\rho^m) - (\rho^{CNT}/\rho^m)w_{CNT}}, \tag{2}$$

where w_{CNT} represents the fraction of mass of the CNTs, and ρ^m and ρ^{CNT} denote densities of the matrix and CNTs, respectively.

Since the effective material properties of CNT-reinforced materials are highly dependent on the structure of CNTs [24–27], an equivalent continuum model based on the Eshelby–Mori–Tanaka approach is employed to estimate the effective material properties of carbon nanotube-reinforced nanocomposites [28–30]. In the light of Benveniste's revision [31], effective elastic module tensor **L** of the panel can be expressed as

$$\mathbf{L} = \mathbf{L}_m + V_{CNT}\langle(\mathbf{L}_{CNT} - \mathbf{L}_m)\cdot\mathbf{A}\rangle\cdot[V_m\mathbf{I} + V_{CNT}\langle\mathbf{A}\rangle]^{-1}, \tag{3}$$

where $\mathbf{L}_{CNT}$ and $\mathbf{L}_m$ are stiffness tensors of CNT and the matrix, respectively. **I** is the fourth-order unit tensor. The angle bracket denotes an average over all possible orientation of the inclusions. **A** is the dilute mechanical strain concentration tensor and is given as

$$\mathbf{A} = \left[\mathbf{I} + \mathbf{S}\cdot\mathbf{L}_m^{-1}\cdot(\mathbf{L}_{CNT} - \mathbf{L}_m)\right]^{-1}, \tag{4}$$

where **S** is the fourth-order Eshelby tensor [30].

3. Theoretical formulations

3.1. Displacement filed and strains

According to the first-order shear deformation shell theory [32], the displacement field is expressed as

$$u(x,\theta,z) = u_0(x,\theta) + z\phi_x(x,\theta), \tag{5}$$

$$v(x,\theta,z) = v_0(x,\theta) + z\phi_\theta(x,\theta), \tag{6}$$

$$w(x,\theta,z) = w_0(x,\theta), \tag{7}$$

where u_0, v_0 and w_0 represent displacements of a point at the middle surface of the panel in x, θ and z directions; ϕ_x and ϕ_θ denote rotations of a transverse normal about positive θ and negative x axes, respectively.

In accordance with the above displacement field, the strain–displacement relations are given as

$$\begin{Bmatrix} \varepsilon_{xx} \\ \varepsilon_{\theta\theta} \\ \gamma_{x\theta} \end{Bmatrix} = \boldsymbol{\varepsilon}_0 + z\boldsymbol{\kappa} = \begin{Bmatrix} \frac{\partial u_0}{\partial x} + \frac{1}{2}\left(\frac{\partial w_0}{\partial x}\right)^2 \\ \frac{\partial v_0}{\partial \theta} + \frac{w_0}{R} + \frac{1}{2}\left(\frac{1}{R}\frac{\partial w_0}{\partial \theta}\right)^2 \\ \frac{1}{R}\frac{\partial u_0}{\partial \theta} + \frac{\partial v_0}{\partial x} + \frac{1}{R}\frac{\partial w_0}{\partial x}\frac{\partial w_0}{\partial \theta} \end{Bmatrix} + z\begin{Bmatrix} \frac{\partial \phi_x}{\partial x} \\ \frac{1}{R}\frac{\partial \phi_\theta}{\partial \theta} \\ \frac{1}{R}\frac{\partial \phi_x}{\partial \theta} + \frac{\partial \phi_\theta}{\partial x} \end{Bmatrix}, \tag{8}$$

$$\begin{Bmatrix} \gamma_{\theta z} \\ \gamma_{xz} \end{Bmatrix} = \boldsymbol{\gamma}_0 = \begin{Bmatrix} \phi_\theta + \frac{1}{R}\frac{\partial w_0}{\partial \theta} - \frac{v_0}{R} \\ \phi_x + \frac{\partial w_0}{\partial x} \end{Bmatrix}. \tag{9}$$

3.2. Energy functional

The strain energy of the CNTRC cylindrical panel is given as

$$U_\varepsilon = \frac{1}{2}\int_0^L \int_0^{\theta_0} \boldsymbol{\varepsilon}^T \mathbf{S}\boldsymbol{\varepsilon} R d\theta dx, \tag{10}$$

where

$$\boldsymbol{\varepsilon} = \begin{Bmatrix} \boldsymbol{\varepsilon}_0 \\ \boldsymbol{\kappa} \\ \boldsymbol{\gamma}_0 \end{Bmatrix}, \tag{11}$$

$$\mathbf{S} = \begin{bmatrix} A_{11} & A_{12} & A_{16} & B_{11} & B_{12} & B_{16} & 0 & 0 \\ A_{12} & A_{22} & A_{26} & B_{12} & B_{22} & B_{26} & 0 & 0 \\ A_{16} & A_{26} & A_{66} & B_{16} & B_{26} & B_{66} & 0 & 0 \\ B_{11} & B_{12} & B_{16} & D_{11} & D_{12} & D_{16} & 0 & 0 \\ B_{12} & B_{22} & B_{26} & D_{12} & D_{22} & D_{26} & 0 & 0 \\ B_{16} & B_{26} & B_{66} & D_{16} & D_{26} & D_{66} & 0 & 0 \\ 0 & 0 & 0 & 0 & 0 & 0 & A^s_{44} & A^s_{45} \\ 0 & 0 & 0 & 0 & 0 & 0 & A^s_{45} & A^s_{55} \end{bmatrix} = \begin{bmatrix} \mathbf{A} & \overline{\mathbf{B}} & \mathbf{0} \\ \overline{\mathbf{B}} & \mathbf{D} & \mathbf{0} \\ \mathbf{0} & \mathbf{0} & \mathbf{A_s} \end{bmatrix}, \tag{12}$$

where the extensional A_{ij}, coupling B_{ij}, bending D_{ij} and transverse shear A^s_{ij} stiffness are calculated by

$$(A_{ij}, B_{ij}, D_{ij}) = \int_{-h/2}^{h/2} Q_{ij}(1, z, z^2)dz, \quad A^s_{ij} = K\int_{-h/2}^{h/2} Q_{ij}\ \mathrm{d}z. \tag{13}$$

The stiffness A_{ij}, B_{ij} and D_{ij} are defined for i,j = 1,2,6 whereas A^s_{ij} is defined for i,j = 4,5. K denotes the transverse shear correction coefficient, which can be computed such that the strain energy due to the transverse shear stresses equals the strain energy due to the true transverse stresses predicted by the 3-D elasticity theory. Q_{ij} are the engineering constants related to the material properties, given as

$$Q_{11} = \frac{E_{11}}{1 - v_{12}v_{21}},\ Q_{22} = \frac{E_{22}}{1 - v_{12}v_{21}},\ Q_{12} = \frac{v_{21}E_{11}}{1 - v_{12}v_{21}}, \tag{14}$$

$$Q_{44} = G_{23},\ Q_{55} = G_{13},\ Q_{66} = G_{12}. \tag{15}$$

With surface traction and body force applied on the panel, the external work is expressed as

$$W_e = \int_0^L \int_0^{\theta_0} \mathbf{u}^T \bar{\mathbf{f}} R d\theta dx + \int_\Gamma \mathbf{u}^T \bar{\mathbf{t}} d\Gamma, \tag{16}$$

where $\bar{\mathbf{f}}$ denotes the external load and $\bar{\mathbf{t}}$ represents the prescribed traction on the natural boundary.

Thus the total potential energy functional of the panels for nonlinear analysis is expressed as

$$\Pi_s = U_\varepsilon - W_e. \tag{17}$$

3.3. Discrete system equations

The construction of kernel particle shape functions has been described in detail by Liu et al. [33] and Chen et al. [34]. Consider a cylindrical panel domain discretized by a set of nodes x_I, $I = 1, \ldots, NP$; the discrete displacement approximations are expressed as

$$\hat{\mathbf{u}} = \sum_{I=1}^{NP} \psi_I(x) \mathbf{u}_I, \tag{18}$$

where $\boldsymbol{u}_I$ is the nodal parameter and $\psi_I(\boldsymbol{x})$ is the shape function related with node I, defined as

$$\psi_I(\boldsymbol{x}) = C(\boldsymbol{x};\ \boldsymbol{x} - \boldsymbol{x}_I)\Phi_a(\boldsymbol{x} - \boldsymbol{x}_I), \tag{19}$$

where $\Phi_a(\boldsymbol{x} - \boldsymbol{x}_I)$ is the kernel function and $C(\boldsymbol{x}; \boldsymbol{x} - \boldsymbol{x}_I)$ is the correction function which can be expressed by a combination of the complete second-order monomial as

$$C(\boldsymbol{x};\ \boldsymbol{x} - \boldsymbol{x}_I) = \mathbf{H}^T(\boldsymbol{x} - \boldsymbol{x}_I)\mathbf{b}(\boldsymbol{x}), \tag{20}$$

$$\mathbf{b}(\boldsymbol{x}) = [b_0(x,\theta), b_1(x,\theta), b_2(x,\theta), b_3(x,\theta), b_4(x,\theta), b_5(x,\theta)]^{\mathrm{T}}, \tag{21}$$

$$\mathbf{H}^{\mathrm{T}}(\boldsymbol{x} - \boldsymbol{x}_I) = [1, x - x_I, \theta - \theta_I, (x - x_I)(\theta - \theta_I), (x - x_I)^2, (\theta - \theta_I)^2]. \tag{22}$$

Thus, Eq. (21) can be rewritten as

$$\psi_I(\boldsymbol{x}) = \mathbf{b}^{\mathrm{T}}(\boldsymbol{x})\mathbf{H}(\boldsymbol{x} - \boldsymbol{x}_I)\Phi_a(\boldsymbol{x} - \boldsymbol{x}_I), \tag{23}$$

$$\psi_I(\boldsymbol{x}) = \mathbf{b}^{\mathrm{T}}(\boldsymbol{x})\mathbf{B}_I(\boldsymbol{x} - \boldsymbol{x}_I), \tag{24}$$

where

$$\mathbf{b}(\boldsymbol{x}) = \mathbf{M}^{-1}(\boldsymbol{x})\mathbf{H}(0), \tag{25}$$

$$\mathbf{B}_I(\boldsymbol{x} - \boldsymbol{x}_I) = \mathbf{H}(\boldsymbol{x} - \boldsymbol{x}_I)\Phi_a(\boldsymbol{x} - \boldsymbol{x}_I), \tag{26}$$

in which

$$\mathbf{M}(\boldsymbol{x}) = \sum_{I=1}^{NP} \mathbf{H}(\boldsymbol{x} - \boldsymbol{x}_I)\mathbf{H}^{\mathrm{T}}(\boldsymbol{x} - \boldsymbol{x}_I)\Phi_a(\boldsymbol{x} - \boldsymbol{x}_I), \tag{27}$$

$$\mathbf{H}(\mathbf{0}) = [1, 0, 0, 0, 0, 0,]^{\mathrm{T}}. \tag{28}$$

The two-dimensional kernel function $\Phi_a(\boldsymbol{x} - \boldsymbol{x}_I)$ is defined as

$$\Phi_a(\boldsymbol{x} - \boldsymbol{x}_I) = \Phi_a(x) \cdot \Phi_a(\theta), \tag{29}$$

where

$$\Phi_a(x) = \varphi\left(\frac{x - x_I}{a}\right). \tag{30}$$

In this paper, the cubic spline function is selected as the weight function, and is given by

$$\varphi_z(z_I) = \left\{ \begin{array}{ll} \frac{2}{3} - 4z_I^2 + 4z_I^3 & \text{for } 0 \leqslant |z_I| \leqslant \frac{1}{2} \\ \frac{4}{3} - 4z_I + 4z_I^2 - \frac{4}{3}z_I^3 & \text{for } \frac{1}{2} < |z_I| \leqslant 1 \\ 0 & \text{otherwise} \end{array} \right\}, \tag{31}$$

where

$$z_I = \frac{x - x_I}{d_I} \tag{32}$$

and d_I is the size of the support of node I which is given as

$$d_I = d_{max} c_I, \tag{33}$$

and d_{max} is a scaling factor ranging from 2.0 to 4.0. In order to avoid the singularity of matrix $\mathbf{M}$, distance c_I is determined by searching for a sufficient number of nodes.

Thus, the shape function can be expressed as

$$\psi_I(\boldsymbol{x}) = \mathbf{H}^{\mathrm{T}}(\mathbf{0})\mathbf{M}^{-1}(\boldsymbol{x})\mathbf{H}(\boldsymbol{x}-\boldsymbol{x}_I)\Phi_a(\boldsymbol{x}-\boldsymbol{x}_I). \tag{34}$$

Eq. (27) can be re-expressed as

$$\mathbf{M}(\boldsymbol{x})\mathbf{b}(\boldsymbol{x}) = \mathbf{H}(0). \tag{35}$$

By using the LU decomposition of matrix $\mathbf{M}(\boldsymbol{x})$, $\mathbf{b}(\boldsymbol{x})$ is determined. Taking the first derivative of Eq. (35), we obtain

$$\mathbf{M}_{,x}(\boldsymbol{x})\mathbf{b}(\boldsymbol{x}) + \mathbf{M}(\boldsymbol{x})\mathbf{b}_{,x}(\boldsymbol{x}) = \mathbf{H}_{,x}(0), \tag{36}$$

which can be rearranged as

$$\mathbf{M}(\boldsymbol{x})\mathbf{b}_{,x}(\boldsymbol{x}) = \mathbf{H}_{,x}(0) - \mathbf{M}_{,x}(\boldsymbol{x})\mathbf{b}(\boldsymbol{x}). \tag{37}$$

It is noted that the first derivative of $\mathbf{b}(\boldsymbol{x})$ can be derived again using the LU decomposition procedure.

Taking the derivative of Eq. (34), the first derivative of the shape function is obtained as

$$\psi_{I,x}(\boldsymbol{x}) = \mathbf{b}_{,x}^{\mathrm{T}}(\boldsymbol{x})\mathbf{B}_I(\boldsymbol{x}-\boldsymbol{x}_I) + \mathbf{b}^{\mathrm{T}}(\boldsymbol{x})\mathbf{B}_{I,x}(\boldsymbol{x}-\boldsymbol{x}_I). \tag{38}$$

Following the same procedure, the second derivative of the shape function can also be obtained.

In the mesh-free method, shape function $\psi_I(\boldsymbol{x})$ does not possess Kronecker delta property. Therefore the essential boundary conditions cannot be imposed directly. In this paper, the transformation method is employed to impose the essential boundary conditions.

Generalized displacement $\tilde{\mathbf{u}}$ is constructed as

$$\tilde{\mathbf{u}}_J = \hat{\mathbf{u}}(x_J) = \sum_{I=1}^{NP} L_{IJ}\mathbf{u}_I, \tag{39}$$

where

$$L_{IJ} = \psi_I(x_J). \tag{40}$$

Eq. (39) can be rewritten as

$$\mathbf{u}_I = \sum_{I=1}^{NP} L_{IJ}^{-T}\tilde{\mathbf{u}}_I. \tag{41}$$

Substituting Eq. (41) into Eq. (39) leads to

$$\hat{\mathbf{u}}_J = \sum_{I=1}^{NP}\psi_I(x_J)\mathbf{u}_I = \sum_{I=1}^{NP}\sum_{K=1}^{NP}\psi_I(\boldsymbol{x})L_{KI}^{-T}\tilde{\mathbf{u}}_K = \sum_{K=1}^{NP}\hat{\psi}_K(\boldsymbol{x})\tilde{\mathbf{u}}_K, \tag{42}$$

where

$$\hat{\psi}_K(x) = \sum_{I=1}^{NP} L_{KI}^{-T}\psi_I(x), \tag{43}$$

Note that

$$\hat{\psi}_I(x_J) = \sum_{I=1}^{NP} L_{IK}^{-T}\psi_K(x_J) = \sum_{I=1}^{NP} L_{IK}^{-T}L_{KJ} = \delta_{IJ}. \tag{44}$$

Therefore, the reconstruction shape function possesses Kronecker delta property.

Substituting discrete displacement Eq. (18) into the total potential energy functional Eq. (17) and taking the variation of the total potential energy functional lead to the discrete system equations

$$\widetilde{\mathbf{K}}(\mathbf{u})\mathbf{u} = \mathbf{F}, \tag{45}$$

where

$$\widetilde{\mathbf{K}}(\mathbf{u}) = \mathbf{K}^L + \mathbf{K}^N(\mathbf{u}) \tag{46}$$

$$\mathbf{u} = [u_1\ u_2\ \ldots\ u_n]^{\mathrm{T}} \tag{47}$$

$$\mathbf{K}^L = \mathbf{K}^b + \mathbf{K}^m + \mathbf{K}^s \tag{48}$$

$$\mathbf{K}^b_{IJ} = \int_0^L \int_0^{\theta_0} \left(\mathbf{B}^b_I\right)^{\mathrm{T}} \mathbf{D}\mathbf{B}^b_J R d\theta dx \tag{49}$$

$$\mathbf{K}^m_{IJ} = \int_0^L \int_0^{\theta_0} \left(\mathbf{B}^m_I\right)^{\mathrm{T}} \mathbf{A}\mathbf{B}^m_J R d\theta dx + \int_0^L \int_0^{\theta_0} \left(\mathbf{B}^m_I\right)^{\mathrm{T}} \overline{\mathbf{B}}\mathbf{B}^b_J R d\theta dx + \int_0^L \int_0^{\theta_0} \left(\mathbf{B}^b_I\right)^{\mathrm{T}} \overline{\mathbf{B}}\mathbf{B}^m_J R d\theta dx, \tag{50}$$

$$\mathbf{K}^s_{IJ} = \int_0^L \int_0^{\theta_0} \left(\mathbf{B}^s_I\right)^{\mathrm{T}} \mathbf{A}^s \mathbf{B}^s_J R d\theta dx, \tag{51}$$

$$\mathbf{K}^N_{IJ} = \int_0^L \int_0^{\theta_0} \left(\frac{1}{2}\mathbf{B}^{L^T}_I \mathbf{S}\mathbf{B}^N_J + \mathbf{B}^{N^T}_I S\mathbf{B}^L_J + \frac{1}{2}\mathbf{B}^{N^T}_I \mathbf{S}\mathbf{B}^N_J\right) R d\theta dx, \tag{52}$$

$$\mathbf{F}_I = \int_0^L \int_0^{\theta_0} \psi_I^T \bar{\mathbf{f}} R d\theta dx + \int_\Gamma \psi_I^T \bar{\mathbf{t}} d\Gamma, \tag{53}$$

in which

$$\mathbf{B}^b_I = \begin{bmatrix} 0 & 0 & 0 & \frac{\partial \psi_I}{\partial x} & 0 \\ 0 & 0 & 0 & 0 & \frac{1}{R}\frac{\partial \psi_I}{\partial \theta} \\ 0 & 0 & 0 & \frac{1}{R}\frac{\partial \psi_I}{\partial \theta} & \frac{\partial \psi_I}{\partial x} \end{bmatrix}, \tag{54}$$

$$\mathbf{B}^m_I = \begin{bmatrix} \frac{\partial \psi_I}{\partial x} & 0 & 0 & 0 & 0 \\ 0 & \frac{1}{R}\frac{\partial \psi_I}{\partial \theta} & \frac{\psi_I}{R} & 0 & 0 \\ \frac{1}{R}\frac{\partial \psi_I}{\partial \theta} & \frac{\partial \psi_I}{\partial x} & 0 & 0 & 0 \end{bmatrix}, \tag{55}$$

$$\mathbf{B}^s_I = \begin{bmatrix} 0 & 0 & \frac{\partial \psi_I}{\partial x} & \psi_I & 0 \\ 0 & -\frac{\psi_I}{R} & \frac{1}{R}\frac{\partial \psi_I}{\partial \theta} & 0 & \psi_I \end{bmatrix}, \tag{56}$$

$$\mathbf{B}^L_I = \begin{bmatrix} \mathbf{B}^m_I \\ \mathbf{B}^b_I \\ \mathbf{B}^s_I \end{bmatrix}, \quad \mathbf{B}^N_I = \overline{\mathbf{H}}\overline{\mathbf{G}}, \tag{57}$$

$$\overline{\mathbf{H}} = \begin{bmatrix} \frac{\partial w}{\partial x} & 0 & \frac{1}{R}\frac{\partial w}{\partial \theta} & 0 & 0 \\ 0 & \frac{1}{R}\frac{\partial w}{\partial \theta} & \frac{\partial w}{\partial x} & 0 & 0 \end{bmatrix}^T, \tag{58}$$

$$\overline{\mathbf{G}}(\mathbf{x}_L) = \begin{bmatrix} 0 & 0 & \frac{\partial \psi_I}{\partial x} & 0 & 0 \\ 0 & 0 & \frac{1}{R}\frac{\partial \psi_I}{\partial \theta} & 0 & 0 \end{bmatrix}. \tag{59}$$

In order to determine the integrations for Eqs. (49)–(53), the bending stiffness matrices are determined using the stabilized nodal integration [35] and other stiffness and force terms are determined using the direct nodal integration [36] instead of the Gauss integration which may reduce the high computational cost and eliminate errors caused by the mismatch between the quadrature cells and the shape function supports [37].

3.4. Solution strategy

To solve the nonlinear system equations, a combination of the arc-length iterative algorithm and the modified Newton–Raphson method are adopted to track the full load–displacement path. The governing Eq. (45) is re-expressed in incremental form as

$$\mathbf{g}(\mathbf{u}) = \widetilde{\mathbf{K}}\mathbf{u} - \mathbf{F} = 0. \tag{60}$$

The applied external load is assumed to be proportional to a fixed load $\mathbf{F}_0$

$$\mathbf{F} = \lambda \mathbf{F}_0. \tag{61}$$

Substituting Eq. (61) into (60), the nonlinear equilibrium equation is rewritten as

$$\mathbf{g}(\mathbf{u},\lambda) = \widetilde{\mathbf{K}}\mathbf{u} - \lambda\mathbf{F}_0 = 0. \tag{62}$$

By changing the external load from $\lambda\mathbf{F}_0$ to $(\lambda + \Delta\lambda)\mathbf{F}_0$, a new equilibrium configuration is obtained

$$\mathbf{g}(\mathbf{u}+\Delta\mathbf{u},\lambda+\Delta\lambda) = 0. \tag{63}$$

Applying the Taylor series expansion to Eq. (63),

$$\mathbf{g}(\mathbf{u}+\Delta\mathbf{u},\lambda+\Delta\lambda) = \mathbf{g}(\mathbf{u},\lambda) + \mathbf{K}_t\Delta\mathbf{u} - \Delta\lambda\mathbf{F}_0 = 0. \tag{64}$$

Taking the first and second order differential of potential energy with displacements, we obtain

$$\frac{\partial U}{\partial u_I} = \widetilde{\mathbf{K}}\mathbf{u}, \tag{65}$$

$$\frac{\partial^2 U}{\partial u_I \partial u_J} = \mathbf{K}_t, \tag{66}$$

where

$$\mathbf{K}_t = \mathbf{K}_0 + \mathbf{K}_n + \mathbf{K}_G, \tag{67}$$

in which $\mathbf{K}_0$ is the linear stiffness matrix and $\mathbf{K}_n$ and $\mathbf{K}_G$ are geometrical stiffness and nonlinear displacement-dependant stiffness matrix, respectively.

The incremental formulae of the equilibrium equation and the displacement are expressed as

$$\Delta\mathbf{u}_m = [\mathbf{K}_t(\mathbf{u}_m)]^{-1}[\Delta\lambda_m\mathbf{F}_0 - \mathbf{g}(\mathbf{u}_m,\lambda_m)] = [\mathbf{K}_t(\mathbf{u}_m)]^{-1}[\Delta\lambda_m\mathbf{F}_0 - \widetilde{\mathbf{K}}(\mathbf{u}_m)\mathbf{u}_m + \lambda_m\mathbf{F}_0], \tag{68}$$

$$\mathbf{u}_{m+1} = \mathbf{u}_m + \Delta\mathbf{u}_m, \tag{69}$$

where m is the load step number.

Since $\Delta\lambda$ is a new variable to be solved, an additional constraint equation is needed for each incremental step. In the present study, the arc-length continuation is used to provide this constraint in which subsequent iterations (denoted by n) are applied for each $\Delta\lambda$ step to reach a new equilibrium. The generalized equations of the incremental-iterative formulae are expressed as

$$\Delta\mathbf{u}_m^n = [(\mathbf{K}_t)_m]^{-1}\left[\Delta\lambda_m^n\mathbf{F}_0 - \mathbf{g}_m^{n-1}\right] = [(\mathbf{K}_t)_m]^{-1}\left[\Delta\lambda_m^n\mathbf{F}_0 - \widetilde{\mathbf{K}}\left(\mathbf{u}_m^{n-1}\right)\mathbf{u}_m + \lambda_m^{n-1}\mathbf{F}_0\right] = \Delta\lambda_m^n[\mathbf{u}_f]_m + [\Delta\mathbf{u}_R]_m^n, \tag{70}$$

$$\mathbf{u}_m^n = \mathbf{u}_m^{n-1} + \Delta\mathbf{u}_m^n, \tag{71}$$

where $[\mathbf{u}_f]_m$ represents one part of the increase in displacement caused by the increase of external load and $[\Delta\mathbf{u}_R]_m^n$ denote the other one from the residual forces. $\Delta\lambda_m^n$ is the increase of the load parameter which can be derived through an iterative arc-length strategy as proposed by Crisfield [38].

4. Numerical results and discussion

Numerical results are presented in this section for large deflection analysis of CNTR-FG cylindrical panels. Poly (methyl methacrylate), referred as PMMA, with material properties $\upsilon_m = 0.34$, $\alpha^m = 45(1 + 0.0005\Delta T) \times 10^{-6}/K$ and $E^m = (3.52 - 0.0034T)$ GPa, where $T = T_0 + \Delta T$ and $T_0 = 300$ K (room temperature) is selected as the matrix. Han and Elliott [39] obtained relatively low values of modulus for (10, 10) SWCNTs ($E_{11}^{CNT} = 600\ GPa$, $E_{22}^{CNT} = 10\ GPa$, $G_{12}^{CNT} = 17.2\ GPa$) since the effective thickness of CNTs was assumed as 0.34 nm. It is reported that the effective thickness of SWCNTs should be smaller than 0.142 nm and the effective wall thickness obtained for (10, 10) SWCNTs is 0.067 nm, which satisfies the Vodenitcharova–Zhang criterion [40]. Thus the material properties reported by Zhang and Shen obtained by MD simulations are used for the present study [41], which is listed in Table 1. For the present element-free method, the kernel particle function is employed to construct the shape functions for the two-dimensional displacement approximations and a scaling factor of 3.1 that represents the size of the support is used in construction of shape functions. Following convergence study, a regular nodal distribution 17 × 17 is chosen.

Table 1
Material properties of (10, 10) SWCNT (L = 9.26 nm, R = 0.68 nm, h = 0.067 nm, $\nu_{12}^{CNT} = 0.175$).

Temperature (K)	E_{11}^{CNT} (TPa)	E_{22}^{CNT} (TPa)	G_{12}^{CNT} (TPa)	$\alpha_{11}^{CNT}(10^{-6}/\mathrm{K})$	$\alpha_{22}^{CNT}(10^{-6}/\mathrm{K})$
300	5.6466	7.0800	1.9445	3.4584	5.1682
500	5.5308	6.9348	1.9643	4.5361	5.0189
700	5.4744	6.8641	1.9644	4.6677	4.8943

4.1. Large deflection analysis of isotropic cylindrical panel

First, large deflection analysis of isotropic cylindrical panel in terms of the number of nodes is provided to demonstrate the validity and accuracy of the proposed method. A fully clamped cylindrical panel under a uniform radial pressure is considered. The boundary conditions are defined as

$$\begin{cases} x = 0, L : u_0 = v_0 = w_0 = \phi_x = \phi_\theta = 0 \\ \theta = 0, \theta_0 : u_0 = v_0 = w_0 = \phi_x = \phi_\theta = 0 \end{cases} \text{(Clamped)}. \tag{72}$$

Geometry and material properties of the panel are: $\theta_0 = 0.2$ rad, $a = 20$ in, $R = 100$ in, $h = 0.125$ in, $E = 4.5 \times 10^5$ psi and $v = 0.3$. As can be seen in Fig. 3, when the cylindrical panel is discretized with 17×17 nodes, the present results are in good agreement with other solutions in the literature [42,43]. According to the accuracy and efficiency, discretization with 17×17 nodes is used for all further analyses.

4.2. Large deflection analysis of CNTR-FG cylindrical panels

Several numerical examples are provided to investigate effects of various parameters on nonlinear behavior of CNTR-FG cylindrical panels in this section. Non-dimensional parameters including $\overline{W} = \frac{W_0}{h}$, $\overline{Z} = \frac{Z}{h}$, $\bar{\sigma}_{xx} = \frac{\sigma_{xx} h^2}{|q_0| a^2}$, $\bar{q} = \frac{q_0 a^4}{E_m h^4}$ (for uniformly distributed load) and $\bar{q} = \frac{q_0 a^2}{E_m h^4}$ (for point load) are defined to describe the results.

Figs. 4 and 5 show variations in the non-dimensional central deflection with load for CNTR-FG cylindrical panels with simply supported and fully clamped boundary conditions subjected to uniformly distributed radial pressure. Simply supported boundary condition is defined as

$$\begin{cases} x = 0, L : v_0 = w_0 = \phi_\theta = 0 \\ \theta = 0, \theta_0 : u_0 = w_0 = \phi_x = 0 \end{cases} \text{(Simply supported)}. \tag{73}$$

Geometric properties of the panels are $\theta_0 = 0.1$ rad, $L = 0.1$ m, $R = 1.0$ m and $h = 0.002$ m. It can be observed that the non-dimensional central deflections rise as the load increases for CNTR-FG cylindrical panels with simply supported and fully clamped boundary conditions. Since the constraint of clamped boundary condition is stronger than simply supported boundary condition, the central deflection of the panels with simply supported four edges is higher than when the edges are clamped. We can also discover that the central deflection for FG-O cylindrical panel has the highest value, while that of FG-X cylindrical panel is the lowest. Therefore, it is concluded that CNTs distributed close to top and bottom surfaces are more efficient in increasing the stiffness of the cylindrical panels than CNTs distributed near the mid-surface. With CNTR-FG cylindrical panels subjected to point load, the corresponding nonlinear responses are illustrated in Figs. 6 and 7. Compared with results of CNTR-FG cylindrical panels subjected to uniformly distributed load, it can be seen that the central deflections increase relatively quickly as the load rises.

Figs. 8–11 show the effect of CNT volume fraction on nonlinear responses of CNTR-FG cylindrical panels with four edges fully clamped boundary conditions subjected to uniformly distributed radial pressure. It can be observed that the non-dimensional central deflections decrease since the stiffness of CNTR-FG cylindrical panels is larger when the proportion of CNT by volume is higher. Some similar effect of the distribution types of CNTs in the panels can also be obtained. Subsequently, two other type CNTR-FG cylindrical panels with different thicknesses are considered ($h = 0.004$ m and $h = 0.008$ m) with $\theta_0 = 0.1$ rad, $L = 0.1$ m and $R = 1.0$ m. Typical results are shown in Figs. 12 and 13.

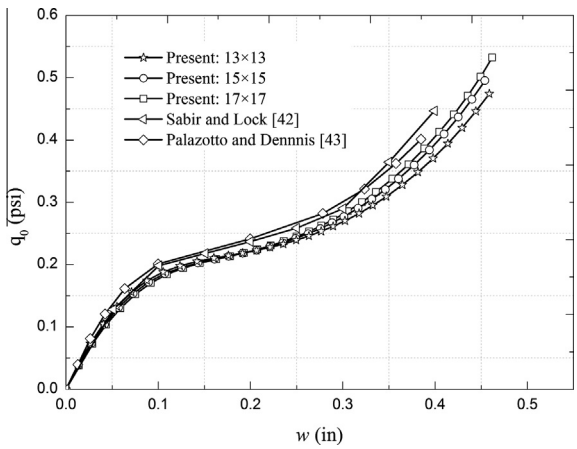

Fig. 3. Convergence property for isotropic cylindrical under uniformly distributed radial pressure.

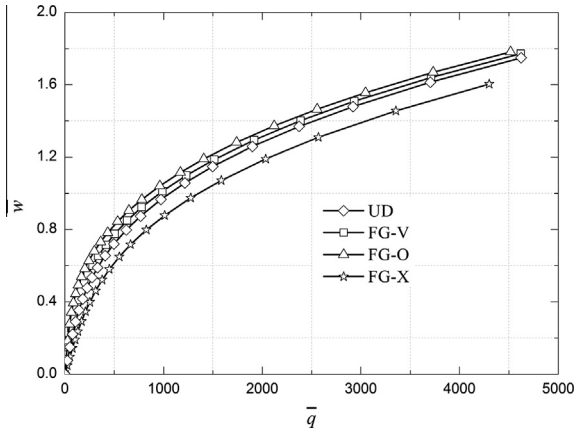

Fig. 4. Variation in the non-dimensional central deflection with load for CNTR-FG cylindrical panels with simply supported boundary condition subjected to uniformly distributed radial pressure.

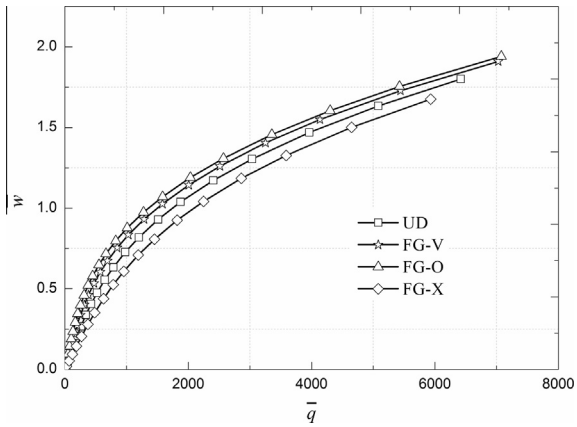

Fig. 5. Variation in the non-dimensional central deflection with load for CNTR-FG cylindrical panels with fully clamped boundary condition subjected to uniformly distributed radial pressure.

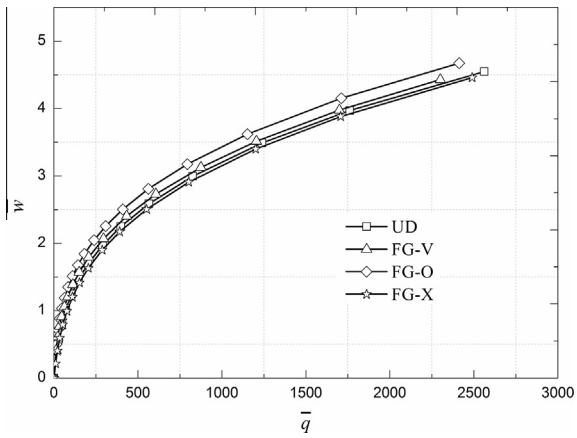

Fig. 6. Variation in the non-dimensional central deflection with load for CNTR-FG cylindrical panels with simply supported boundary condition subjected to point load.

Figs. 14–17 depict effect of span angle (θ_0) on non-dimensional load–deflection curves of CNTR-FG cylindrical panels with four edges fully clamped boundary conditions subjected to uniformly distributed radial pressure. It can be seen that the

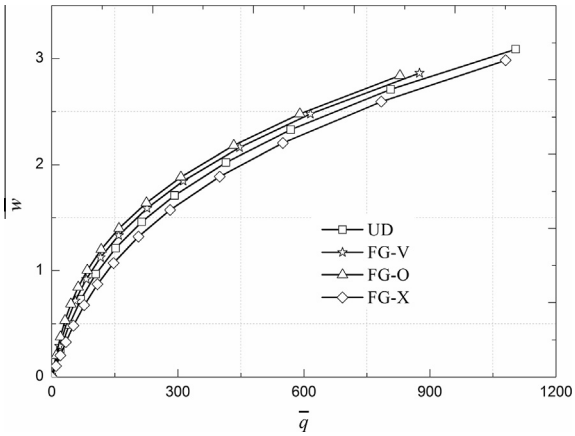

Fig. 7. Variation in the non-dimensional central deflection with load for CNTR-FG cylindrical panels with fully clamped boundary condition subjected to point load.

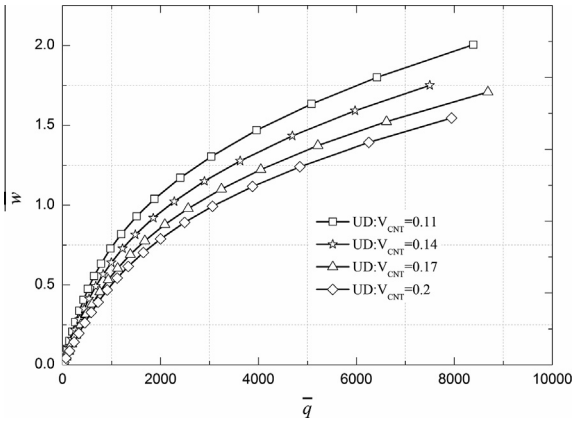

Fig. 8. Effect of CNT volume fraction on nonlinear response of UD CNTRC cylindrical panels with four edges fully edges clamped boundary conditions subjected uniformly distributed radial pressure.

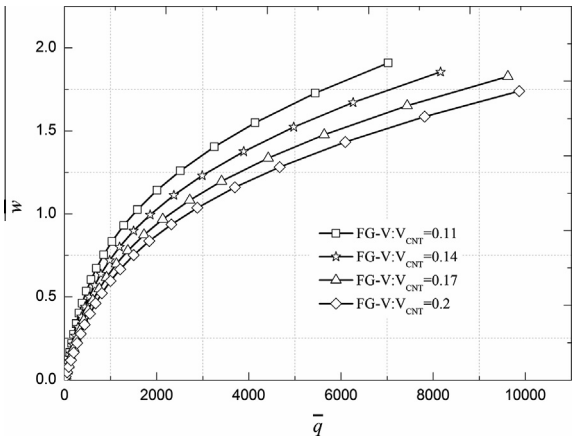

Fig. 9. Effect of CNT volume fraction on nonlinear response of FG-V CNTRC cylindrical panels with four edges fully edges clamped boundary conditions subjected uniformly distributed radial pressure.

central deflections increase more and more slowly as the span angle changes from 0.1 to 1.0. Therefore we conclude that when CNTR-FG cylindrical panels subjected to uniformly distributed radial pressure, having the same geometry, it is harder to deform the panels with larger span angle.

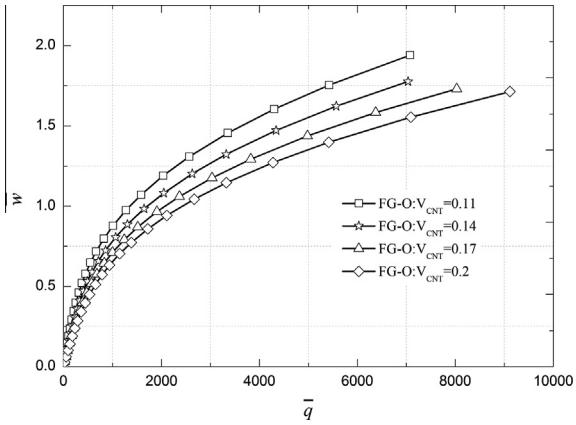

Fig. 10. Effect of CNT volume fraction on nonlinear response of FG-O CNTRC cylindrical panels with four edges fully edges clamped boundary conditions subjected uniformly distributed radial pressure.

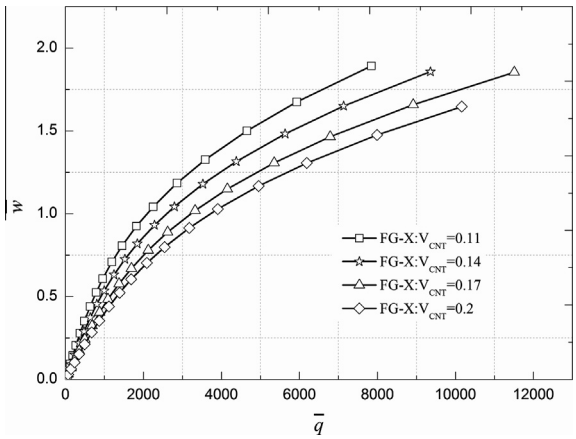

Fig. 11. Effect of CNT volume fraction on nonlinear response of FG-X CNTRC cylindrical panels with four edges fully edges clamped boundary conditions subjected uniformly distributed radial pressure.

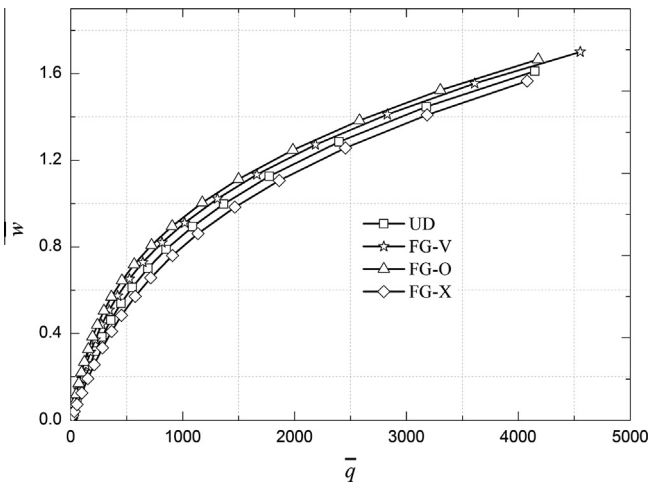

Fig. 12. Variation in the non-dimensional central deflection with load for CNTR-FG cylindrical panels with fully clamped boundary condition subjected to uniformly distributed radial pressure (h = 0.004).

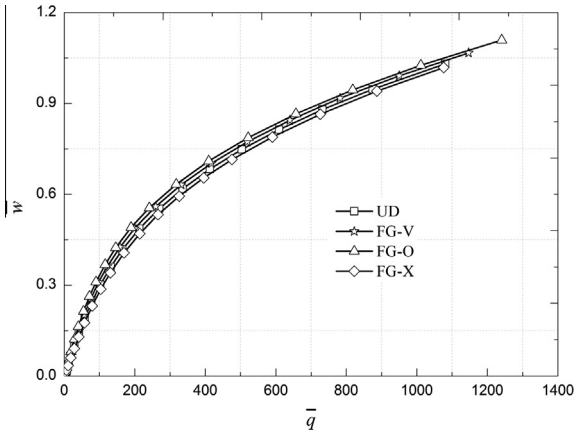

Fig. 13. Variation in the non-dimensional central deflection with load for CNTR-FG cylindrical panels with fully clamped boundary condition subjected to uniformly distributed radial pressure (h = 0.008).

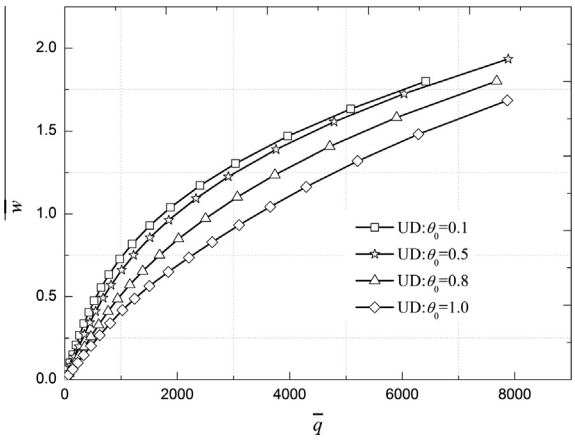

Fig. 14. Effect of span angle on nonlinear response of UD CNTRC cylindrical panels with four edges fully edges clamped boundary conditions subjected uniformly distributed radial pressure.

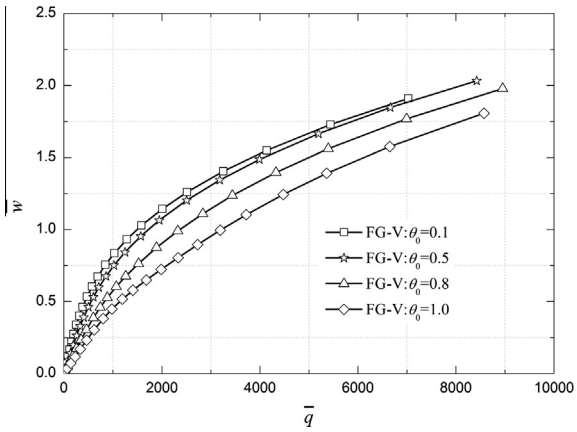

Fig. 15. Effect of span angle on nonlinear response of FG-V CNTRC cylindrical panels with four edges fully edges clamped boundary conditions subjected uniformly distributed radial pressure.

Figs. 18–21 show variations in the non-dimensional central deflection with load for CNTR-FG cylindrical panels with different edge-to-radius ratios (L/R). It can be seen that as the load rises, central deflections of CNTR-FG cylindrical panels with

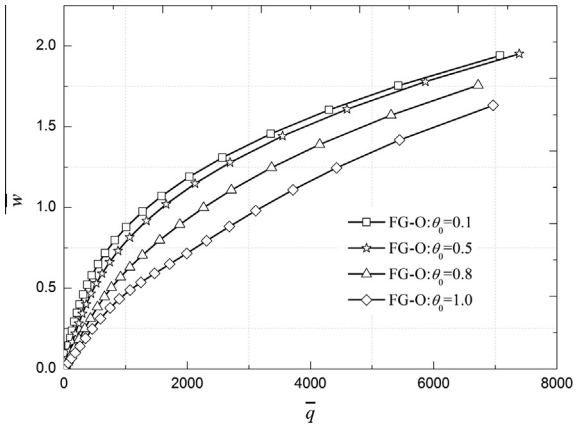

Fig. 16. Effect of span angle on nonlinear response of FG-O CNTRC cylindrical panels with four edges fully edges clamped boundary conditions subjected uniformly distributed radial pressure.

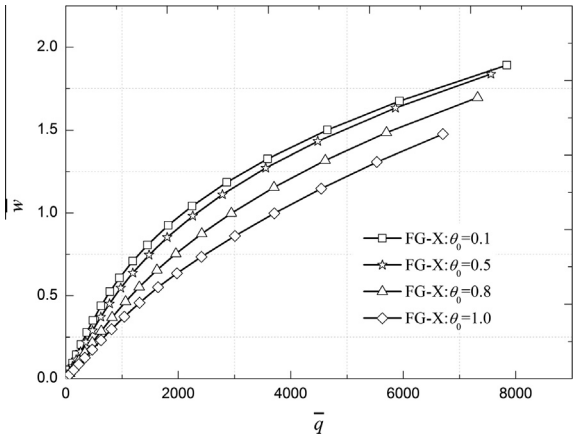

Fig. 17. Effect of span angle on nonlinear response of FG-X CNTRC cylindrical panels with four edges fully edges clamped boundary conditions subjected uniformly distributed radial pressure.

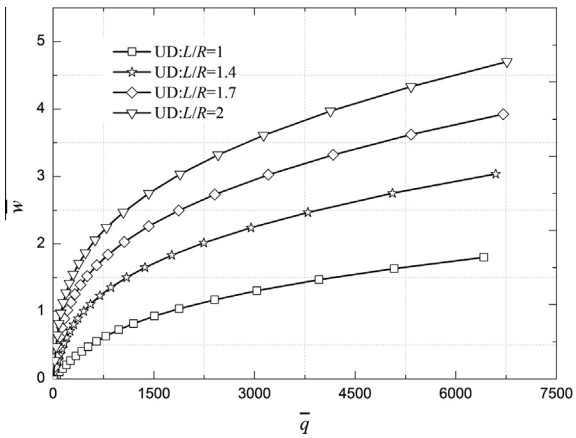

Fig. 18. Effect of edge-to-radius ratio on nonlinear response of UD CNTRC cylindrical panels with four edges fully edges clamped boundary conditions subjected uniformly distributed radial pressure.

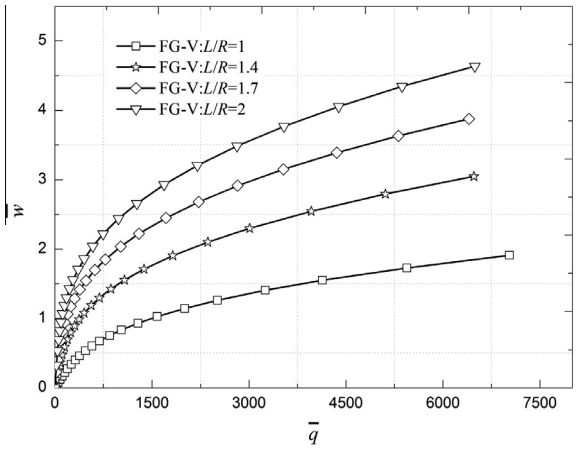

Fig. 19. Effect of edge-to-radius ratio on nonlinear response of FG-V CNTRC cylindrical panels with four edges fully edges clamped boundary conditions subjected uniformly distributed radial pressure.

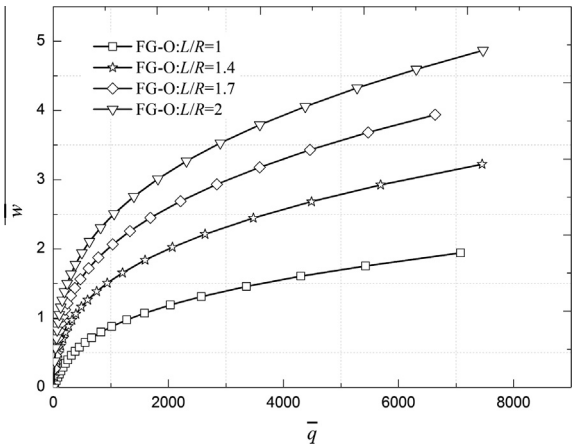

Fig. 20. Effect of edge-to-radius ratio on nonlinear response of FG-O CNTRC cylindrical panels with four edges fully edges clamped boundary conditions subjected uniformly distributed radial pressure.

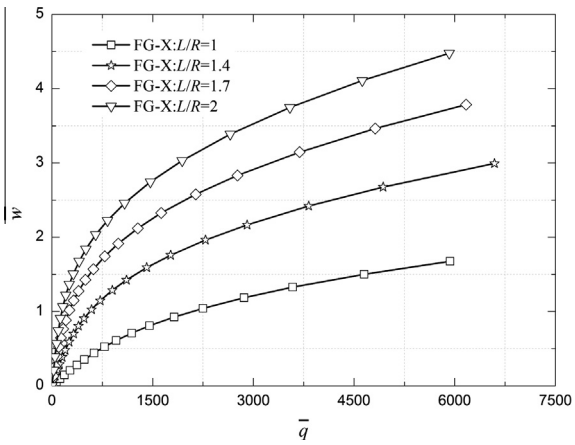

Fig. 21. Effect of edge-to-radius ratio on nonlinear response of FG-X CNTRC cylindrical panels with four edges fully edges clamped boundary conditions subjected uniformly distributed radial pressure.

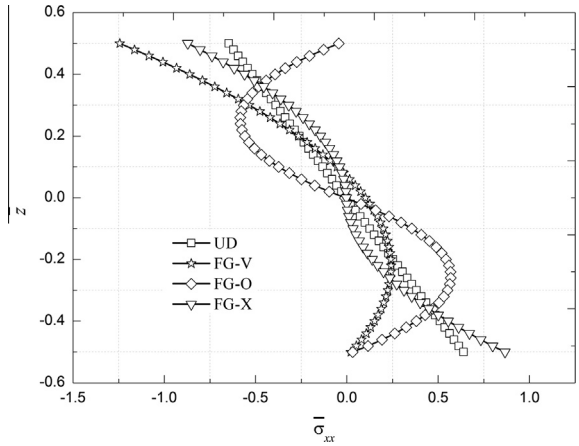

Fig. 22. Non-dimensional central axial stresses $\bar{\sigma} = \frac{\sigma_{xx}h^2}{|q_0|a^2}$ distributed along the non-dimensional thickness $\bar{z} = \frac{z}{h}$ of for CNTR-FG cylindrical panels with simply supported boundary condition subjected to uniformly distributed radial pressure $q_0 = 1.0 \times 10^7$ N/m^2.

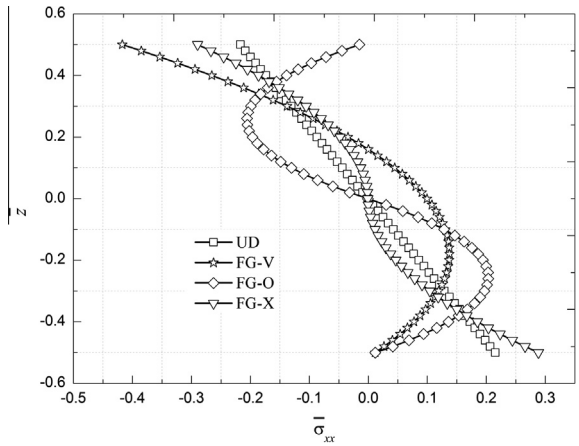

Fig. 23. Non-dimensional central axial stresses $\bar{\sigma} = \frac{\sigma_{xx}h^2}{|q_0|a^2}$ distributed along the non-dimensional thickness $\bar{z} = \frac{z}{h}$ of for CNTR-FG cylindrical panels with fully clamped boundary condition subjected to uniformly distributed radial pressure $q_0 = 1.0 \times 10^7$ N/m^2.

larger edge-to-radius ratios (L/R), increase relatively quickly. That is to be expected because it is obvious that longer CNTR-FG cylindrical panels are easily deformed when subjected to uniformly distributed radial pressure. Compared with effects of CNT volume fraction, thickness and span angle, we can also obtain that the nonlinear behavior of CNTR-FG cylindrical panels is more sensitive to edge-to-radius ratio (L/R).

Figs. 22 and 23 depicts the non-dimensional central axial stresses $\bar{\sigma}_{xx} = \frac{\sigma_{xx}h^2}{|q_0|a^2}$ distributed along the non-dimensional thickness $\overline{Z} = \frac{Z}{h}$ for CNTR-FG cylindrical panels with simply supported and fully clamped boundary conditions, subjected to uniformly distributed radial pressure $q_0 = 1.0 \times 10^7$ N/m^2. Since the reinforcements are symmetric about the mid-surface for UD, FG-O and FG-X panels and the panels are very thin, we can discover that the central axial stresses are zero at mid-surface and anti-symmetric about the mid-surface. For FG-V panel, it can be seen that the central axial stresses are not anti-symmetric or symmetric about the mid-surface and zero stress surface moves near to upper surface.

5. Conclusions

In this paper, a first attempt to use the mesh-free kp-Ritz method for large deflection geometrically nonlinear analysis of CNTR-FG cylindrical panels subjected to mechanical loads is performed. CNTs are assumed to be graded in thickness direction of the cylindrical panel and effective material properties are estimated through a micromechanical model based on the Eshelby–Mori–Tanaka approach. The formulation is based on the first-order shear deformation shell theory. The two-dimensional displacement field is approximated by the mesh-free kernel particles estimate. To improve the computational efficiency and eliminate shear and membrane locking, a stabilized conforming nodal integration scheme is employed to

evaluate the system's bending stiffness and the membrane and shear terms are calculated by the direct nodal integration method. A combination of the arc-length iterative algorithm and the modified Newton–Raphson method is adopted to solve the nonlinear system equations to track the full load–displacement path. Several numerical examples are presented to figure out the effects of various parameters including volume fraction of CNTs, edge-to-radius ratio, span angle and thickness on nonlinear responses of the panels. The influence of boundary conditions and distribution types of CNTs in the cylindrical panels is also examined.

Acknowledgment

The work described in this paper was fully supported by a Grant from the China National Natural Science Foundation (Grant No. 51378448).

References

[1] K. Liao, S. Li, Interfacial characteristics of a carbon nanotube-polystyrene composite system, Appl. Phys. Lett. 79 (2001) 4225–4227.
[2] M. Wong, M. Paramsothy, X.J. Xu, Y. Ren, S. Li, K. Liao, Physical interactions at carbon nanotube-polymer interface, Polymer 44 (2003) 7757–7764.
[3] D. Qian, E.C. Dickey, R. Andrews, T. Rantell, Load transfer and deformation mechanisms in carbon nanotube-polystyrene composites, Appl. Phys. Lett. 76 (2000) 2868–2870.
[4] G.M. Odegard, T.S. Gates, K.E. Wise, C. Park, E.J. Siochi, Constitutive modeling of nanotube–reinforced polymer composites, Compos. Sci. Technol. 63 (2003) 1671–1687.
[5] X.L. Gao, K. Li, A shear-lag model for carbon nanotube-reinforced polymer composites, Int. J. Solids Struct. 42 (2005) 1649–1667.
[6] C. Li, T.W. Chou, Multiscale modeling of compressive behavior of carbon nanotube/polymer composites, Compos. Sci. Technol. 66 (2006) 2409–2414.
[7] G.D. Seidel, D.C. Lagoudas, Micromechanical analysis of the effective elastic properties of carbon nanotube reinforced composites, Mech. Mater. 38 (2006) 884–907.
[8] J. Wuite, S. Adali, Deflection and stress behaviour of nanocomposite reinforced beams using a multiscale analysis, Compos. Struct. 71 (2005) 388–396.
[9] M.H. Yas, N. Samadi, Free vibrations and buckling analysis of carbon nanotube-reinforced composite Timoshenko beams on elastic foundation, Int. J. Press. Vessels Pip. 98 (2012) 119–128.
[10] M. Rafiee, J. Yang, S. Kitipornchai, Large amplitude vibration of carbon nanotube reinforced functionally graded composite beams with piezoelectric layers, Compos. Struct. 96 (2013) 716–725.
[11] P. Zhu, Z.X. Lei, K.M. Liew, Static and free vibration analyses of carbon nanotube-reinforced composite plates using finite element method with first order shear deformation plate theory, Compos. Struct. 94 (2012) 1450–1460.
[12] G. Formica, W. Lacarbonara, R. Alessi, Vibrations of carbon nanotube-reinforced composites, J. Sound Vib. 329 (2010) 1875–1889.
[13] Z.X. Lei, K.M. Liew, J.L. Yu, Large deflection analysis of functionally graded carbon nanotube-reinforced composite plates by the element-free kp-Ritz method, Comput. Methods Appl. Mech. Eng. 256 (2013) 189–199.
[14] Z.X. Lei, K.M. Liew, J.L. Yu, Buckling analysis of functionally graded carbon nanotube-reinforced composite plates using the element-free kp-Ritz method, Compos. Struct. 98 (2013) 160–168.
[15] Z.X. Lei, K.M. Liew, J.L. Yu, Free vibration analysis of functionally graded carbon nanotube-reinforced composite plates using the element-free kp-Ritz method in thermal environment, Compos. Struct. 106 (2013) 128–138.
[16] K.M. Liew, Z.X. Lei, J.L. Yu, L.W. Zhang, Postbuckling of carbon nanotube-reinforced functionally graded cylindrical panels under axial compression using a meshless approach, Comput. Methods Appl. Mech. Eng. 268 (2014) 1–17.
[17] Z.X. Lei, J.L. Yu, K.M. Liew, Free vibration analysis of functionally graded carbon nanotube-reinforced composite cylindrical panels, Compos. Struct. 1 (2013) 36–40.
[18] Z.X. Wang, H.S. Shen, Nonlinear vibration of nanotube-reinforced composite plates in thermal environments, Comput. Mater. Sci. 50 (2011) 2319–2330.
[19] B.S. Aragh, A.H.N. Barati, H. Hedayati, Eshelby–Mori–Tanaka approach for vibrational behavior of continuously graded carbon nanotube-reinforced cylindrical panels, Compos. Part B 43 (2012) 1943–1954.
[20] H.S. Shen, Y. Xiang, Nonlinear vibration of nanotube-reinforced composite cylindrical shells in thermal environments, Comput. Methods Appl. Mech. Eng. 213–216 (2012) 196–205.
[21] H.S. Shen, Thermal buckling and postbuckling behavior of functionally graded carbon nanotube-reinforced composite cylindrical shells, Compos. Part B 43 (2012) 1030–1038.
[22] H.S. Shen, Postbuckling of nanotube-reinforced composite cylindrical shells in thermal environments, Part I: Axially-loaded shells, Compos. Struct. 93 (2011) 2096–2108.
[23] H.S. Shen, Postbuckling of nanotube-reinforced composite cylindrical shells in thermal environments, Part II: Pressure-loaded shells, Compos. Struct. 93 (2011) 2496–2503.
[24] X. Li, H. Gao, W.A. Scrivens, D. Fei, X. Xu, M.A. Sutton, A.P. Reynolds, M.L. Myrick, Reinforcing mechanisms of single-walled carbon nanotube-reinforced polymer composites, J. Nanosci. Nanotechnol. 7 (2007) 2309–2317.
[25] A.M.K. Esawi, M.M. Farag, Carbon nanotube reinforced composites: potential and current challenges, Mater. Des. 28 (2007) 2394–2401.
[26] G.D. Seidel, D.C. Lagoudas, Micromechanical analysis of the effective elastic properties of carbon nanotube reinforced composites, Mech. Mater. 38 (2006) 884–907.
[27] V. Anumandla, R.F. Gibson, A comprehensive closed form micromechanics model for estimating the elastic modulus of nanotube-reinforced composites, Compos. Part A 37 (2006) 2178–2185.
[28] T. Mori, K. Tanaka, Average stress in matrix and average elastic energy of materials with misfitting inclusions, Acta Metall. 21 (1973) 571–574.
[29] J.D. Eshelby, The elastic field outside an ellipsoidal inclusion, Proc. R. Soc. Lond. Ser. A 252 (1959) 561–569.
[30] J.D. Eshelby, The determination of the elastic field of an ellipsoidal inclusion, and related problems, Proc. R. Soc. Lond. Ser. A 241 (1957) 376–396.
[31] Y. Benveniste, A new approach to the application of Mori–Tanaka's theory in composite materials, Mech. Mater. 6 (1987) 147–157.
[32] J.N. Reddy, Mechanics of Laminated Composite Plates and Shells: Theory and Analysis, second ed., CRC Press, Boca Raton, FL, 2004.
[33] W.K. Liu, S. Jun, Y.F. Zhang, Reproducing kernel particle methods, Int. J. Numer. Method Fluids 20 (1995) 1081–1106.
[34] J.S. Chen, C. Pan, C.T. Wu, W.K. Liu, Reproducing kernel particle methods for large deformation analysis of non-linear structures, Comput. Methods Appl. Mech. Eng. 139 (1996) 195–227.
[35] J.S. Chen, C.T. Wu, S. Yoon, Y. You, A stabilized conforming nodal integration for Galerkin mesh-free methods, Int. J. Numer. Methods Eng. 50 (2001) 435–466.
[36] J. Dolbow, T. Belytschko, Numerical integration of the Galerkin weak form in meshfree methods, Comput. Mech. 23 (1999) 219–230.
[37] S. Beissel, T. Belytschko, Nodal integration of the element-free Galerkin method, Comput. Methods Appl. Mech. Eng. 139 (1996) 49–74.
[38] M.A. Crisfield, Nonlinear Finite Element Analysis of Solids and Structures, John Wiley & Sons, Chichester, UK, 1991.

[39] Y. Han, J. Elliott, Molecular dynamics simulations of the elastic properties of polymer/carbon nanotube composites, Comput. Mater. Sci. 39 (2007) 315–323.
[40] C.Y. Wang, L.C. Zhang, A critical assessment of the elastic properties and effective wall thickness of single-walled carbon nanotubes, Nanotechnology 19 (2008) 075075.
[41] H.S. Shen, C.L. Zhang, Thermal buckling and postbuckling behavior of functionally graded carbon nanotube-reinforced composite plates, Mater. Des. 31 (2010) 3403–3411.
[42] A.B. Sabir, A.C. Lock, The application of finite elements to the large deflection geometrically nonlinear behaviour of cylindrical shell, Variational Methods in Engineering, Southampton Press, UK, 1972.
[43] A.N. Palazotto, D. ST, Nonlinear Analysis of Shell Structures, AIAA, Washington, DC, 1992.